

Analysis of Photocurrent Generation within a Schottky-Junction-Based Near-Field Thermophotovoltaic System

Jaeman Song, Mikyung Lim, Seung S. Lee, and Bong Jae Lee*

Department of Mechanical Engineering, Korea Advanced Institute of Science and Technology, Daejeon 34141, South Korea



(Received 24 December 2018; revised manuscript received 8 March 2019; published 12 April 2019)

Numerous studies have reported performance enhancement of thermophotovoltaic (TPV) systems when an emitter is separated by nanoscale gaps from a TPV cell. Although *p-n*-junction-based TPV cells have been widely used for near-field TPV systems, Schottky-junction-based near-field TPV systems have drawn attention recently with the advantage of easy fabrication. However, existing studies mostly focused on the generated photocurrent only in the metal side due to the fact that required energy for the metal-side photocurrent (i.e., Schottky barrier height) is smaller than the band-gap energy. Here, we suggest a precise performance analysis model for Schottky-junction-based near-field TPV systems, including photocurrent generation on the semiconductor side by considering the transport of minority carriers within the semiconductor. It is found that most of the total photocurrent in Schottky-junction-based near-field TPV systems is generated in the semiconductor side. We also demonstrate that further enhancement in photocurrent generation can be achieved by reabsorbing the usable photon energy in the metal with the help of a back-side reflector. The present work provides a design guideline for Schottky-junction-based near-field TPV systems, taking into account three types of photocurrents.

DOI: 10.1103/PhysRevApplied.11.044040

I. INTRODUCTION

Thermophotovoltaic (TPV) systems have widely received attention as a promising energy conversion device that directly converts the absorbed thermal radiation into electricity with the advantages of quiet operation and the potential for miniaturization [1–3]. As one way to further improve the performance of TPV systems, near-field radiation has been applied (i.e., near-field TPV systems). When the vacuum-gap distance between the emitter and the receiver is smaller than the thermal characteristic wavelength determined by Wien's displacement law [4], the magnitude of radiative heat transfer can surpass the black-body limit through the coupling of evanescent waves (i.e., photon tunneling) [5]. In fact, it has already been shown that performance enhancement of TPV systems can be achieved by reducing the gap between the emitter and the TPV cell [6–14].

One representative structure of the TPV cell is a *p-n* junction semiconductor and there have been extensive theoretical works regarding *p-n*-junction-based near-field TPV systems [6,7,9–12,14,15]. Under illumination of photons with a wavelength shorter than the wavelength corresponding to the band gap of the semiconductor, electron-hole pairs are generated inside the semiconductor, diffused toward the depletion region and separated by the

built-in electric field across the region, which yields the net current flow (i.e., photocurrent generation) [16]. Recently, the enhanced performance of a near-field TPV system was experimentally demonstrated using a *p-n*-junction-based TPV cell made of InAs [17]; however, challenges in fabricating a perfectly flat *p-n* junction TPV cell, as well as its high cost and high band-gap energy, make experimental demonstration rather limited [13,17,18].

Alternatively, the Schottky junction can also be utilized as a TPV system [8,13,19,20] and it can be formed when a metal, which has a greater work function than the electron affinity of a semiconductor, makes contact with the semiconductor [16]. Compared to the *p-n* junction, the Schottky junction has an advantage in the simple fabrication process because there is no need for high-temperature and expensive fabrication steps like diffusion and annealing [21,22]. Furthermore, through the simplified fabrication process, surface conditions (e.g., cleanliness, roughness, and planarity) of the TPV cell can be well controlled such that the nanoscale vacuum gap between the emitter and the TPV cell can be maintained relatively easier than the case of the *p-n*-junction-based TPV cell. Further, the Schottky-junction-based TPV cell is also able to produce the metal-side photocurrent (i.e., internal photoemission photocurrent) by absorbing a photon with less energy than the band-gap energy of semiconductor, making it advantageous when the band-gap energy is greater than that of the absorbed radiation.

*bongjae.lee@kaist.ac.kr

Accordingly, all the previous studies on the Schottky-junction-based near-field TPV system have mainly analyzed the electrical power generation from the metal side because they employed a semiconductor with a high band-gap energy (e.g., silicon) [8,13,19]. However, the significance of photocurrent generation from the semiconductor side of a Schottky-junction-based TPV cell has been emphasized continuously [16,23–25] and several studies have even suggested that, in order to obtain a high photocurrent density, the absorption of the incident photon by the metal should be minimized because the quantum efficiency of the internal photoemission photocurrent is marginal [16]. Although recent works have demonstrated that the quantum efficiency of the internal photoemission photocurrent can be improved depending on various factors, such as the fabrication conditions, the geometry of the metallic layer, and surface plasmon polaritons [16,26–29], it is crucial to contemplate the photocurrent generation from the semiconductor side when designing a near-field TPV system. For example, if we employ a low-band-gap semiconductor (e.g., GaSb, InSb, or InAs) and an appropriate metal for the Schottky junction, the generated photocurrent from the semiconductor side can also contribute to the total generated photocurrent, meaning that there is room for significantly improving the performance of the Schottky-junction-based near-field TPV system.

In this work, we propose a model for predicting the performance of a Schottky-junction-based near-field TPV system and we analyze the performance accordingly with the basic configuration. Tungsten is used as an emitter and a nickel-*n*-doped GaSb Schottky-junction-based TPV cell is selected as a receiver. Photocurrents generated from either side are compared and a proper thickness of the metal for an enhanced performance is discussed. Furthermore, additional performance improvement is achieved by introducing the backside reflector, which can increase the photocurrent generation from the metal side.

II. MODEL AND METHOD

Figure 1(a) illustrates a schematic of the Schottky-junction-based near-field TPV system. As an emitter, tungsten is maintained at 1000 K. The Schottky-junction-based TPV cell maintained at 300 K is located with a vacuum-gap distance d from the emitter. In order to make the Schottky junction, a 5-nm-thick nickel layer is deposited on the *n*-doped GaSb, which is the verified configuration in the recent experimental work [20].

In order to calculate the absorbed net radiative heat flux in each layer of the Schottky-junction-based TPV cell, formulations for the near-field thermal radiation between multilayered structures considering both forward and backward waves in each layer are employed [6,30]. The net radiative heat flux can be expressed as $q''_{\text{net}} = \int_0^\infty d\lambda q''_{\lambda, \text{net}} = \int_0^\infty d\lambda \int_0^\infty S_{\beta, \lambda}(\beta, \lambda) d\beta$, where λ refers to

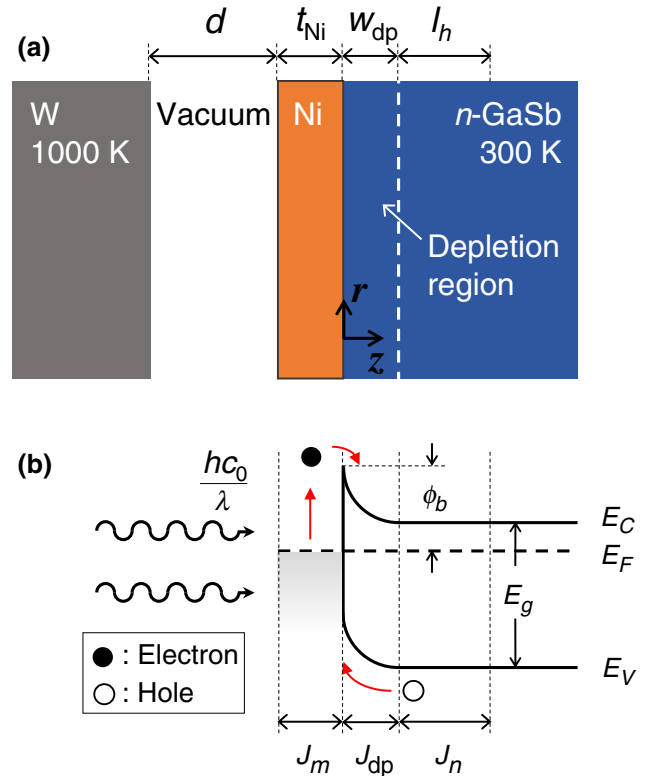


FIG. 1. (a) Schematic of a Schottky-junction-based near-field TPV system consisting of a tungsten emitter and a nickel-deposited *n*-doped GaSb TPV cell. (b) Energy-band diagram for the Schottky-junction-based TPV cell.

vacuum wavelength, β is the parallel wavevector component, and the expression for the $S_{\beta, \lambda}(\beta, \lambda)$ can be found in Refs. [6,30]. The permittivity values of bulk tungsten and bulk gold for $\lambda < 10 \mu\text{m}$ are obtained from the tabular data in Ref. [31]. For $\lambda > 10 \mu\text{m}$, their permittivity values are estimated from the Lorentz-Drude (LD) oscillator model [32]. For the nickel, the thickness-dependent dielectric function is estimated by modifying the scattering rate of the Drude model [32] (see Appendix A for details). The band-gap energy E_g of the *n*-doped GaSb is calculated as 0.72 eV using Varshini's equation [33]. For $E \geq E_g$, where the interband absorption is dominant, its dielectric function is estimated using the model suggested by Adachi [34], while, for $E < E_g$, Patrini's Lorentz-Drude model [35], which considers the absorption contribution by the lattice and free carrier, is used. Both Adachi's and Patrini's models are independent of the doping concentration.

A. Power generation in the Schottky-junction-based TPV cell

In order to make the Schottky junction, the work function of the metal and the electron affinity of the semiconductor should be considered first. The work function of a

metal ϕ_m is defined as the energy difference between the vacuum level and the Fermi level. The electron affinity of a semiconductor χ is the energy difference between the vacuum level and the conduction band. When a high-work-function metal and a low-electron-affinity semiconductor make a contact, the ideal Schottky barrier height, $\phi_b = \phi_m - \chi$, is formed after lining up the Fermi levels on both materials [16]. The Schottky-junction-based TPV cell used in this work (i.e., Ni/n-doped GaSb) has $\phi_b = 0.4976$ eV [20]. On the other hand, if a low-work-function metal and a high-electron-affinity semiconductor are used to make a contact, then an ohmic junction is formed, which can be used for an electrode or a backside reflector because of its low electrical junction resistance [16].

When a metal and a semiconductor make a contact, a depletion region is formed adjacent to the metal layer so that the built-in electric field is formed [refer to Fig. 1(a)]. The 90.4-nm-thick depletion region w_{dp} is yielded for the considered nickel-*n*-doped GaSb junction using Poisson's equation under the approximation of an abrupt junction (see Appendix B for details) [16,36,37]. We further assume that the depletion region is formed in the *n*-GaSb side and regard the remaining part of the *n*-GaSb as a neutral region.

As illustrated in the energy-band diagram of the Schottky-junction-based TPV system [refer to Fig. 1(b)], electron transport from the metal to the semiconductor can contribute to the photocurrent generation. In addition, the movement of holes from the semiconductor to the metal can also generate the photocurrent. The photocurrents generated in each layer are noted as J_m (i.e., in the metal layer); J_{dp} (i.e., in the depletion region); and J_n (i.e., in the neutral region), respectively.

When the photon whose energy is greater than the Schottky barrier height (ϕ_b) is absorbed in the metal layer, the photoexcited hot electron can be emitted to the semiconductor side. Using the emission probability, which is determined by momentum analysis of the hot electron based on the constructed wavevector-space sphere and the escape cone, the internal photoemission quantum efficiency $\eta_{m,\lambda}$ is estimated [26]. This model is derived by assuming the ballistic transport of initial photoexcited hot electrons. Please note that when the thickness of a metal film is smaller than the attenuation length (i.e., 3.2 nm for Ni [38]), a thin-film model is employed by considering the multiple reflections of a hot carrier within the thin metal film (see Sec. 1 of Supplemental Material 1 for details [39]). Photoexcited electrons produce the spectral internal photoemission photocurrent $J_{m,\lambda}$ that can be calculated using the following equation:

$$J_{m,\lambda}(\lambda) = \eta_{\lambda,m} e \frac{q''_{\lambda,m}}{hc_0/\lambda}, \quad \text{with } \frac{hc_0}{\lambda} \geq \phi_b, \quad (1)$$

where $q''_{\lambda,m}$ is the spectral radiative heat flux absorbed in the metal, h is the Planck constant, e is the electron charge, and c_0 is the speed of light in vacuum.

When the photon whose energy is greater than the band-gap energy (E_g) passes through the metal layer and is absorbed in the semiconductor, an electron-hole pair is generated inside the semiconductor. In this situation, the diffused and swept minority carriers produce diffusion and drift photocurrents, respectively [6,7,10,16]. In the neutral region of GaSb, within the diffusion length of holes (l_h), the diffusion photocurrent is generated when the minority carrier diffuses and reaches the depletion region. The following one-dimensional steady-state continuity equation is used to calculate the concentration of the diffused minority carrier $n_h(z, \lambda)$ considering the recombination [6,7,10]:

$$D_h \frac{d^2}{dz^2} \left[n_h(z, \lambda) - n_h^0 \right] - \frac{n_h(z, \lambda) - n_h^0}{\tau_h} + \dot{g}(z, \lambda) = 0, \quad (2)$$

where $\dot{g}(z, \lambda) = -dQ_\lambda(z, \lambda)/dz \times \lambda/hc_0$ is the spectral photogeneration rate of electron-hole pairs with $Q_\lambda(z, \lambda) = \int_0^\infty S_{\beta,\lambda,SC}(\beta, \lambda) e^{-2\beta(k_{z,SC})^2} d\beta$ being the net radiative heat flux inside the TPV cell. Note that $S_{\beta,\lambda,SC}$ indicates the $S_{\beta,\lambda}$ absorbed in the semi-infinite semiconductor and $k_{z,SC}$ is the z -component wavevector, while the subscript "SC" represents the semiconductor. In Eq. (2), n_h^0 is the equilibrium hole concentration, D_h is the diffusion coefficient, and τ_h is the lifetime of holes. Here, $n_h(z, \lambda) - n_h^0$ is solved by employing the semianalytic method [10] with the following boundary conditions: (i) the hole concentration is assumed to be equilibrium at the edge of the depletion region (i.e., $n_h = n_h^0$ at $z = w_{dp}$) and (ii) surface recombination is neglected in the region farther than the diffusion length from the depletion region edge [i.e., $D_h(dn_h/dz)|_{z=w_{dp}+3l_h} = 0$]. The spectral hole diffusion photocurrent can then be calculated by

$$J_{n,\lambda}(\lambda) = -e D_h \frac{dn_h(z, \lambda)}{dz} \Big|_{z=w_{dp}} \quad \text{with } \frac{hc_0}{\lambda} \geq E_g, \quad (3)$$

where the diffusion coefficient of *n*-doped GaSb, $D_h = 19 \text{ cm}^2 \text{s}^{-1}$, is taken from Ref. [33] when $N_D = 1 \times 10^{17} \text{ cm}^{-3}$. The lifetime of a hole, $\tau_h = 30 \text{ ns}$, at a given N_D is calculated by considering the radiative recombination and nonradiative [Auger and Shockley-Read-Hall (SRH)] recombination processes [7,33]. With those values, the hole diffusion length is estimated to be $7.5 \mu\text{m}$ from $l_h = \sqrt{D_h \tau_h}$ [6].

In the depletion region, because the minority carriers (i.e., holes for the *n* type) are swept by the built-in electric field, the spectral drift photocurrent is assumed to be generated without any recombination (i.e., quantum efficiency

of 100%) [6,7,10]. It can be expressed by

$$J_{dp,\lambda}(\lambda) = e \frac{Q_\lambda(0, \lambda) - Q_\lambda(w_{dp}, \lambda)}{hc_0/\lambda}, \quad \text{with } \frac{hc_0}{\lambda} \geq E_g, \quad (4)$$

where $Q_\lambda(0, \lambda) - Q_\lambda(w_{dp}, \lambda)$ represents the spectral radiative heat flux absorbed in the depletion region.

Finally, the spectral photocurrent density $J_{ph,\lambda}(\lambda)$ is calculated by the summation of the generated spectral photocurrents in each layer, i.e., $J_{ph,\lambda}(\lambda) = J_{m,\lambda}(\lambda) + J_{dp,\lambda}(\lambda) + J_{n,\lambda}(\lambda)$, and the total photocurrent J_{ph} can be obtained from the integration of the spectral photocurrent: $J_{ph} = \int J_{ph,\lambda}(\lambda) d\lambda$. Under illumination, the current-voltage characteristics of the Schottky TPV cell can be defined by subtracting the dark current from the total photocurrent J_{ph} :

$$J = J_{ph} - A^* T^2 \exp\left(-\frac{e\phi_b}{k_B T}\right) \left[\exp\left(\frac{eV}{k_B T}\right) - 1 \right], \quad (5)$$

where $A^* = 5.16 \times 10^4 \text{ Am}^{-2} \text{ K}^{-2}$ is the Richardson constant of the n -doped GaSb [20]. The dark current of the Schottky TPV cell expressed as the second term of the right side of Eq. (5) is obtained from the current-voltage characteristics of the Schottky diode considering the thermionic

emission of carriers [16]. The maximum electrical power output of the TPV system is calculated as the maximum product of current and voltage related with Eq. (5). The validation of the suggested performance analysis model of the Schottky-junction-based near-field TPV system is described in Sec. 2 of Supplemental Material 2 [39] by comparing the measured data from a previously conducted experiment [20] with our numerical simulation result.

III. RESULTS AND DISCUSSION

Let us first consider the amount of radiative heat flux absorbed in each layer of the Schottky TPV cell. Figure 2(a) shows the absorbed radiative heat flux with $\lambda < \lambda_g$ in each layer with respect to the vacuum-gap distance d . Outside the hole diffusion length of the neutral region of the TPV cell, the generated electron-hole pair rarely contributes to the diffusion photocurrent; thus, it is simply noted as “waste” in Fig. 2. It can be seen from Fig. 2(a) that the 5-nm-thick nickel layer absorbs more radiative energy than the 90.4-nm-thick depletion region for all considered d values. However, the absorbed radiative heat flux in the neutral region within the diffusion length of GaSb is greater than that in the nickel film. Magnitudes of the absorbed radiative heat flux in the metal film and in the neutral region within the diffusion length become comparable only at the extremely small vacuum

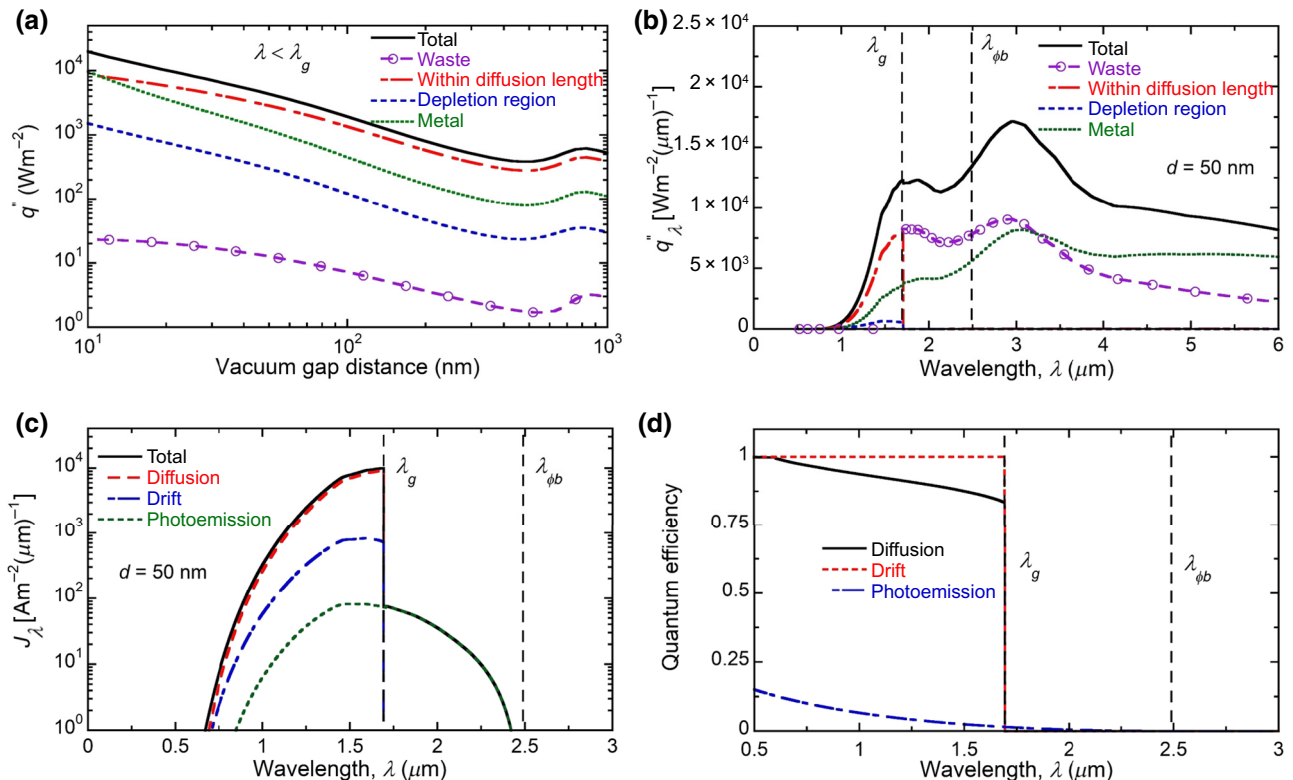


FIG. 2. (a) Absorbed radiative heat flux with $\lambda < \lambda_g$ in each layer of the Schottky TPV cell. (b) Spectral heat flux q''_λ when $d = 50$ nm. (c) Spectral photocurrent J_λ when $d = 50$ nm. (d) Quantum efficiency of three generated photocurrents in the Schottky TPV cell.

gap (i.e., $d = 10$ nm) as a result of the short radiation penetration depth at such a small gap [40,41]. Thus, it can be inferred that the photocurrent generation in the semiconductor side cannot be neglected unless the thickness of metal film is much thicker than the radiation penetration depth at moderate vacuum-gap distances of $d > 50$ nm.

Figure 2(b) shows the absorbed spectral heat flux in each layer at $d = 50$ nm. Here, we consider the vacuum-gap distance of $d = 50$ nm according to the recently reported near-field TPV experiment [17]. For $\lambda > \lambda_g$, the radiative heat flux is rarely absorbed in the depletion region nor in the neutral region within the diffusion length, suggesting that most of the absorbed radiation in the semi-infinite GaSb semiconductor for this spectral regime is simply wasted. On the other hand, the nickel layer absorbs a wide spectral range of the radiative heat flux, and the corresponding internal photoemission photocurrent ($J_{m,\lambda}$) can be produced even at wavelengths longer than the band-gap wavelength as long as the absorbed photon has greater energy than the Schottky barrier height (i.e., $\lambda < \lambda_{\phi_b}$). The amount of absorbed energy that is useful for the metal layer (i.e., $\lambda < \lambda_{\phi_b}$) is larger than that for the neutral region within the diffusion length (i.e., $\lambda < \lambda_g$).

Figure 2(c) shows the log-scaled spectral photocurrent density generated in the three different layers: the neutral region (i.e., diffusion photocurrent); depletion region (i.e., drift photocurrent); and metal layer (i.e., internal photoemission photocurrent) at $d = 50$ nm. In this condition, the obtained total photocurrent density is 3372 Am^{-2} and maximum electrical power output is 246 Wm^{-2} . This resultant power output is 25 times greater than that of the far-field TPV at a $5\text{-}\mu\text{m}$ -gap distance (see Fig. S3 of Supplemental Material 3 [39] and Ref. [42] for details). It can be clearly seen that the internal photoemission photocurrent can be generated in a wider spectral range than the drift and the diffusion photocurrents. However, J_m accounts for only about 1.8% of J_{ph} , although the absorbed useful radiation in the metal side is greater than that in the neutral region within the diffusion length. This result is due to the low quantum efficiency of the internal photoemission photocurrent compared to that of the drift or diffusion photocurrent in the semiconductor, as can be seen in Fig. 2(d). As mentioned in the previous section, the drift quantum efficiency is assumed to be 100% and the diffusion quantum efficiency, which is obtained from $\eta_{n,\lambda} = J_{n,\lambda} \times hc_0/e\lambda \times 1/[Q_\lambda(w_{dp}, \lambda) - Q_\lambda(w_{dp} + l_h, \lambda)]$, is larger than 0.8 for $\lambda < \lambda_g$. However, $\eta_{m,\lambda} < 0.2$ in the wavelength of interest ($0.5 \text{ }\mu\text{m} < \lambda < \lambda_{\phi_b}$) and becomes almost negligible in $\lambda_g < \lambda < \lambda_{\phi_b}$, which makes the internal photoemission photocurrent marginal compared to the drift and the diffusion photocurrents [see Fig. 2(c)]. This result is because the thick-film model, i.e., $\eta_{m,\lambda} = \frac{1}{2} (1 - \sqrt{\lambda_{\phi_b}/hc_0})^2$, is employed when the metal layer is thicker than the attenuation length (i.e., 3.2 nm for Ni [38]). The further

description about the $\eta_{m,\lambda}$ depending on the metal layer thickness and attenuation length is described in Fig. S1 of Supplemental Material 1 [39]. Consequently, the photocurrent generated in the semiconductor cannot be neglected as previously done in Ref. [20]. If the temperature of the tungsten becomes higher, the performance of the TPV cell can be further improved due to the increase of the magnitude of the radiative heat flux as well as the blueshift of the spectral radiative heat flux (see Fig. S4 of Supplemental Material 3 [39]). On the other hand, for a given emitter temperature, using a thinner nickel layer would be beneficial for enhancing the photocurrent generation of the considered Schottky-junction-based near-field TPV system.

Figures 3(a) and 3(b) describe the spectral radiative heat flux absorbed in the metal and in the semiconductor

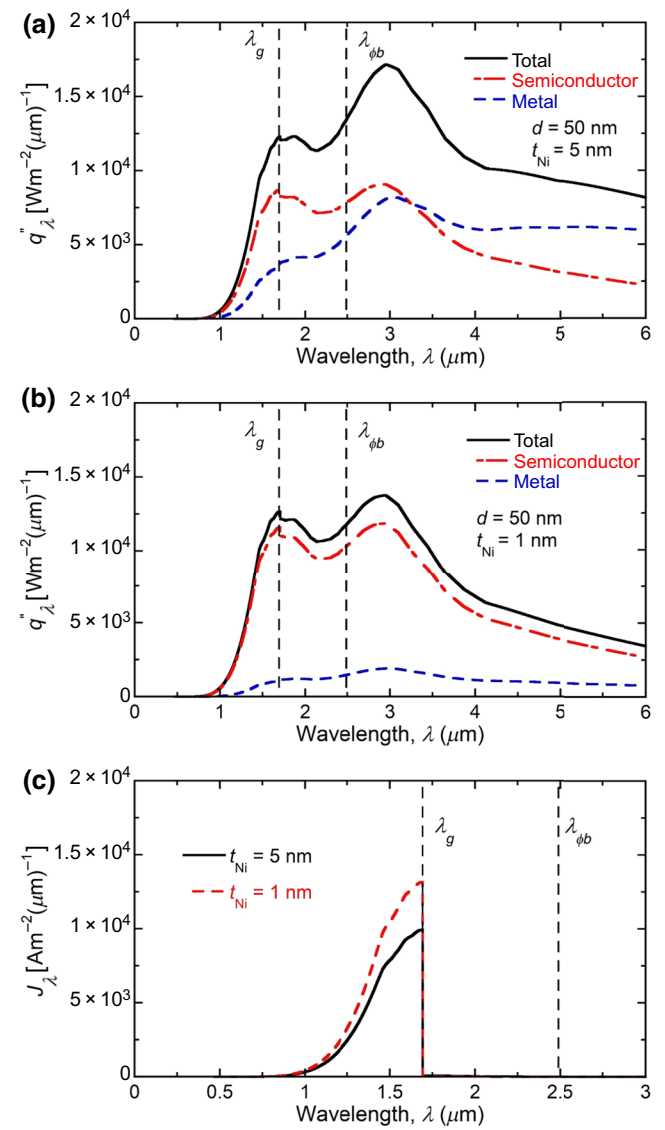


FIG. 3. (a),(b) Spectral heat flux q''_λ when $t_{Ni} = 5$ and 1 nm, respectively. (c) Comparison of the net spectral photocurrent for both cases.

when $t_{\text{Ni}} = 5$ and 1 nm, respectively, at $d = 50$ nm. When $t_{\text{Ni}} = 5$ nm in Fig. 3(a), the absorbed radiative energy in the metal layer is 1.95 times greater than that in the semiconductor. As t_{Ni} decreases to 1 nm [see Fig. 3(b)], the absorption in the metal layer decreases, such that only 18% of the total radiative heat flux is absorbed by the metal layer. Although the total radiative heat flux decreases as t_{Ni} decreases, the configuration with the 1-nm-thick nickel layer yields a larger photocurrent [see Fig. 3(c)]. This result is because for the thinner Ni configuration, the photons whose energy is greater than the band-gap energy can be absorbed more in the semiconductor side (i.e., having high quantum efficiency) rather than in the metal side (i.e., having low quantum efficiency). By decreasing the thickness of the Ni layer to 1 nm, the total photocurrent is increased by 1.3 times and the maximum electrical power is enhanced by 1.4 times compared to the case with the 5-nm-thick nickel layer. Furthermore, because the total radiative heat flux also decreases, the conversion efficiency

(i.e., the maximum power output divided by the total radiative heat flux absorbed in the TPV cell) increases 2.7 times with the 1-nm-thick nickel layer.

It can be readily seen from Figs. 2 and 3 that a significant portion of the radiative heat flux absorbed in the semiconductor does not produce the photocurrent. This process can result in the rise of the cell temperature (i.e., thermal loss), which may increase the dark current and deteriorate the performance of near-field TPV system. In order to deal with the wasted heat absorbed in the n -doped GaSb, a thin Au film that can form ohmic contact with GaSb can be introduced at the bottom of the TPV cell. To do so, the thickness of the GaSb semiconductor is set to be 5 μm considering the penetration depth (approximately 1 μm) of the spectral near-field radiative heat flux in $\lambda < \lambda_g$. Figure 4(a) describes the spectral heat flux absorbed in the semiconductor and in metal with or without the Au-backside reflector. Because Au has a high reflectivity in the infrared spectral region, photons that

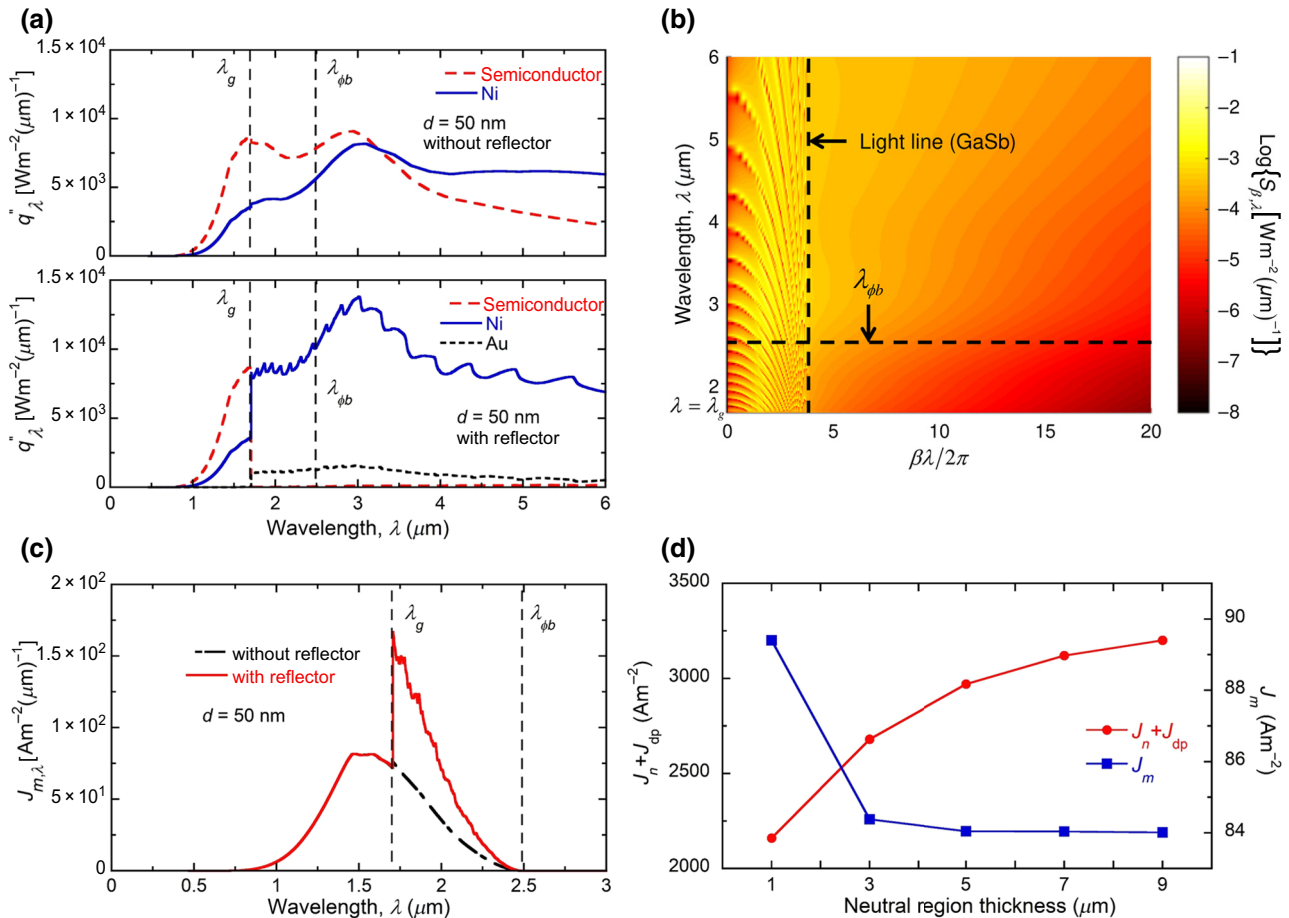


FIG. 4. (a) Spectral heat flux q''_λ without (upper panel) or with (lower panel) the backside reflector. (b) Contour plot of $S_{\beta,\lambda}(\beta, \lambda)$ absorbed in the nickel layer. The x axis indicates the normalized parallel wavevector and the vertically dashed line indicates the GaSb light line inside of which the wave propagates in the GaSb TPV cell at $0 < \beta\lambda/2\pi < n_{\text{GaSb}}$. (c) Spectral photocurrent $J_{m,\lambda}$ with or without the backside reflector. (d) Total photocurrent density generated in the semiconductor ($J_n + J_{dp}$) and metal side (J_m) with respect to the thickness of the neutral region.

reach the Au-backside reflector (mostly $\lambda > \lambda_g$) can be effectively reflected back. Considering that GaSb rarely absorbs the radiative heat flux in the spectral region of $\lambda > \lambda_g$, the absorption in the finite-thickness GaSb layer in this wavelength interval is significantly reduced, as also noted in Refs. [14,43]. Interestingly, the absorbed energy for $\lambda > \lambda_g$ in the nickel metal layer significantly increases with the Au-backside reflector.

To elucidate the physical mechanism of the increased absorption in the Ni layer due to the Au-backside reflector, the contour of $S_{\beta,\lambda}$ absorbed in the nickel layer is plotted in Fig. 4(b). Because of the multiple reflections between Ni and Au, Fabry-Perot-like resonance modes appear inside the GaSb light line. The enhanced absorption due to the Fabry-Perot-like resonances occurs more densely in the wavelength-wavevector space for the thicker GaSb. Because the spectral radiative flux above the Schottky barrier height can be reabsorbed by the nickel layer, the resulting spectral internal photoemission photocurrent for $\lambda_g < \lambda < \lambda_{\phi_b}$ can increase significantly [refer to Fig. 4(c)], leading to the 1.4-times enhancement in J_m . However, the 1.4-times enhancement in J_m by adding the backside reflector cannot enhance the power output significantly because the contribution of the internal photoemission photocurrent to the photocurrent generation is negligible. Moreover, both the spectral heat flux and the spectral photocurrent at $\lambda < \lambda_g$ will not change much because most of the radiative heat flux with the energy greater than the band-gap energy will be absorbed before reaching the Au reflector. Therefore, the Au-backside reflector results in no enhancement in the conversion efficiency due to the reabsorption of the radiative heat flux in the nickel layer.

To investigate the effects of the thickness of the neutral region on the performance of the Schottky-junction-based near-field TPV system, the photocurrent density is calculated for different thicknesses of the neutral region in Fig. 4(d). Here, the finite difference method is used to calculate the photocurrent generated in the finite-thickness semiconductor instead of the semianalytic method. The boundary condition at the interface between the semiconductor and the Au reflector is $D_h(dn_h/dz)|_{z=w_{dp}+w_n} = -u_n [n_h(w_{dp} + w_n) - n_h^0]$, where $u_n = 10,000 \text{ ms}^{-1}$ is the surface recombination velocity [44] and w_n is the thickness of the neutral region. It can be seen from Fig. 4(d) that the thinner neutral region results in less generated photocurrent in the semiconductor side (i.e., $J_n + J_{dp}$). This result is due to the increased minority carrier loss caused by the surface recombination at the GaSb-Au interface. If the thickness of the neutral region further decreases and becomes comparable to or smaller than the radiation penetration depth, the internal photoemission photocurrent can be increased because the radiative energy greater than the band gap ($\lambda < \lambda_g$) can be reflected back and reabsorbed in the Ni layer. In fact, Fig. 4(d) clearly shows that J_m , which was nearly constant in $3 \mu\text{m} < w_n < 9 \mu\text{m}$, is significantly

improved as w_n decreases to $1 \mu\text{m}$. However, because the increase of J_m is much smaller than the reduction of $J_n + J_{dp}$, reducing w_n is not advantageous if the quantum efficiency for the internal photoemission photocurrent is extremely low.

According to Ref. [26], if one employs an extremely thin metal layer (i.e., thinner than the 5 nm considered here) and uses materials whose attenuation length is longer than nickel (e.g., silver [45]), the quantum efficiency of the internal photoemission photocurrent can be improved. As a limiting case, when the ratio of the attenuation length to the thickness of the metal layer becomes infinite, all electrons having energy greater than ϕ_b can surmount the Schottky barrier height, resulting in the quantum efficiency $\eta_{m,\lambda} = 1 - \lambda\phi_b/hc_0$ (i.e., the infinitely-thin-film model; see Sec. 1 of Supplemental Material 1 [39]). If we assume such a limiting case for the system with a $1\text{-}\mu\text{m}$ -thick neutral region (introducing the Au reflector), the internal photoemission photocurrent (2360 Am^{-2}) can be the same order of magnitude as the diffusion photocurrent (1756 Am^{-2}), leading to 2.44-times enhancement in the power output and the conversion efficiency (i.e., an increase from 146 to 357 W m^{-2} with an infinitely-thin-film model). In addition, several previous studies suggested that the quantum efficiency for the internal photoemission photocurrent can overcome the limit of $\eta_{m,\lambda} = 1 - \lambda\phi_b/hc_0$ if the hot carrier is generated by surface plasmon polaritons (SPPs) [27,28]. The SPPs supported in the thin metal can be coupled to the SPPs supported in the emitter, which may lead to significant enhancement of the absorbed radiation in both the metal side and the semiconductor side of the TPV cell. Therefore, considering all types of photocurrent generation in the Schottky-junction near-field TPV system is crucial in designing a system with high performance.

IV. CONCLUSIONS

The performance of Schottky-junction-based near-field TPV systems is investigated with a detailed model considering photocurrent generation in the semiconductor side of the TPV cell. When the vacuum-gap distance between the tungsten emitter and the nickel-*n*-doped GaSb Schottky-junction-based TPV cell is 50 nm, the ratio of generated diffusion, drift, and internal photoemission photocurrents is found to be 1:0.12:0.02, meaning that the photocurrent generation in the semiconductor side takes most of the photocurrent generation in the Schottky-junction-based TPV cell. Resultant power output is 246 W m^{-2} , which is 25 times greater than that of the far-field TPV system. It is found that depositing the thinner nickel layer is advantageous to enhance the performance of the near-field TPV system. Further, it is shown that by introducing the back-side reflector, the radiative heat flux with energy greater than the Schottky barrier height can be reabsorbed in the Ni

layer, and the corresponding internal photoemission photocurrent increases 1.4 times. In order to obtain remarkable enhancement in the power output with the backside reflector, the quantum efficiency of the internal photoemission photocurrent should be improved first by modifying the metal geometry or employing the hot-carrier generation accompanied with the SPPs. The quantitative study presented here shows that the role of the semiconductor is crucial in analyzing the performance of Schottky-junction-based near-field TPV systems and will promote future study and implementation of near-field TPV systems.

ACKNOWLEDGMENTS

This research is supported by the Basic Science Research Program (Grants No. NRF-2017R1A2B2011192 and No. NRF-2019R1A2C2003605), as well as by the Creative Materials Discovery Program (Grant No. NRF-2018M3D1A1058972) through the National Research Foundation of Korea (NRF) funded by Ministry of Science and ICT.

APPENDIX A: THICKNESS-DEPENDENT DIELECTRIC FUNCTION FOR NICKEL

The thickness-dependent dielectric function of Ni is defined by modifying the intraband effects (i.e., Drude model) of the Lorentz-Drude oscillator model [32] given that the dielectric function in the infrared range is dominated by the contribution of free electrons [46]. The modified Drude model is expressed as the following equation [47–49]:

$$\varepsilon(\omega) = \varepsilon_{\text{bulk}}(\omega) + \Omega_p^2 \left(\frac{1}{\omega^2 + \Gamma_0^2} - \frac{1}{\omega^2 + \Gamma^2} \right) - i \frac{\Omega_p^2}{\omega} \left(\frac{\Gamma_0}{\omega^2 + \Gamma_0^2} - \frac{\Gamma}{\omega^2 + \Gamma^2} \right), \quad (\text{A1})$$

where $\varepsilon_{\text{bulk}}(\omega)$ is the permittivity of bulk Ni, Ω_p is the plasma frequency, and Γ_0 is the scattering rate of bulk Ni listed in Ref. [32]. $\Gamma = \Gamma_0 + v_F/t_{\text{Ni}}$ is the scattering rate of thin Ni, where $v_F = 2.34 \times 10^5 \text{ ms}^{-1}$ is the Fermi velocity of Ni [50] and t_{Ni} is the thickness of Ni film.

APPENDIX B: DETERMINATION OF A DEPLETION REGION WIDTH

The width of the depletion region w_{dp} is determined using the following equation:

$$w_{\text{dp}} = \sqrt{\frac{2\varepsilon_s}{eN_D} (\psi_{\text{BI}} - V_f)}, \quad (\text{B1})$$

where $\varepsilon_s = 1.390 \times 10^{-10} \text{ F m}^{-1}$ is the static permittivity of the GaSb [33], $N_D = 1 \times 10^{17} \text{ cm}^{-3}$ is the n -doping

concentration, e is the electron charge, and V_f is the forward bias. The built-in potential ψ_{BI} is obtained from [16,36]

$$\psi_{\text{BI}} = \phi_b - (E_C - E_F). \quad (\text{B2})$$

In Eq. (B2), for the nondegenerate semiconductor, the difference between conduction level E_C and Fermi level E_F is calculated by $E_C - E_F = k_B T \ln(N_C/N_D)$, where k_B is the Boltzmann constant and T is the temperature of the TPV cell. Because the effective density of states in the conduction band, $N_C = 2.806 \times 10^{17} \text{ cm}^{-3}$, is larger than N_D , the considered n -doped GaSb can be regarded as the nondegenerate semiconductor [16]. We also assume that n -doped GaSb is fully ionized given that the thermal energy $k_B T$ is comparable to the ionization energy at 300 K [16]. With the assumption that variation of the width of the depletion region by forward bias can be neglected (i.e., $V_f = 0$), Eq. (B1) yields a 90.4-nm-thick depletion region for the considered nickel- n -doped GaSb junction.

- [1] S. Basu, Y.-B. Chen, and Z. M. Zhang, Microscale radiation in thermophotovoltaic devices: A review, *Int. J. Energy Res.* **31**, 689 (2007).
- [2] K. Park and Z. Zhang, Fundamentals and applications of near-field radiative energy transfer, *Front. Heat Mass Transf.* **4**, 013001 (2013).
- [3] E. Tervo, E. Bagherisereshki, and Z. Zhang, Near-field radiative thermoelectric energy converters: A review, *Front. Energy* **12**, 5 (2018).
- [4] T. L. Bergman, F. P. Incropera, D. P. DeWitt, and A. S. Lavine, *Fundamentals of Heat and Mass Transfer* (John Wiley & Sons, New York, 2011), 7th ed.
- [5] S. Basu, *Near-field Radiative Heat Transfer across Nanometer Vacuum Gaps: Fundamentals and Applications* (William Andrew, Norwich, 2016).
- [6] K. Park, S. Basu, W. P. King, and Z. M. Zhang, Performance analysis of near-field thermophotovoltaic devices considering absorption distribution, *J. Quant. Spectrosc. Radiat. Transfer* **109**, 305 (2008).
- [7] M. Francoeur, R. Vaillon, and M. P. Mengüç, Thermal impacts on the performance of nanoscale-gap thermophotovoltaic power generators, *IEEE Trans. Energy Convers.* **26**, 686 (2011).
- [8] V. B. Svetovoy and G. Palasantzas, Graphene-on-Silicon Near-field Thermophotovoltaic Cell, *Phys. Rev. Appl.* **2**, 034006 (2014).
- [9] M. P. Bernardi, O. Dupré, E. Blandre, P.-O. Chapuis, R. Vaillon, and M. Francoeur, Impacts of propagating, frustrated and surface modes on radiative, electrical and thermal losses in nanoscale-gap thermophotovoltaic power generators, *Sci. Rep.* **5**, 11626 (2015).
- [10] M. Lim, S. Jin, S. S. Lee, and B. J. Lee, Graphene-assisted Si-InSb thermophotovoltaic system for low temperature applications, *Opt. Express* **23**, A240 (2015).
- [11] J. K. Tong, W.-C. Hsu, Y. Huang, S. V. Boriskina, and G. Chen, Thin-film ‘thermal well’ emitters and absorbers

- for high-efficiency thermophotovoltaics, *Sci. Rep.* **5**, 10661 (2015).
- [12] S. Jin, M. Lim, S. S. Lee, and B. J. Lee, Hyperbolic metamaterial-based near-field thermophotovoltaic system for hundreds of nanometer vacuum gap, *Opt. Express* **24**, A635 (2016).
- [13] R. St-Gelais, G. R. Bhatt, L. Zhu, S. Fan, and M. Lipson, Hot carrier-based near-field thermophotovoltaic energy conversion, *ACS Nano* **11**, 3001 (2017).
- [14] M. Lim, J. Song, J. Kim, S. S. Lee, I. Lee, and B. J. Lee, Optimization of a near-field thermophotovoltaic system operating at low temperature and large vacuum gap, *J. Quant. Spectrosc. Radiat. Transf.* **210**, 35 (2018).
- [15] A. Karalis and J. D. Joannopoulos, ‘‘Squeezing’’ near-field thermal emission for ultra-efficient high-power thermophotovoltaic conversion, *Sci. Rep.* **6**, 28472 (2016).
- [16] S. M. Sze and K. K. Ng, *Physics of Semiconductor Devices* (John Wiley & Sons, Chichester, 2006), 3rd ed.
- [17] A. Fiorino, L. Zhu, D. Thompson, R. Mittapally, P. Reddy, and E. Meyhofer, Nanogap near-field thermophotovoltaics, *Nat. Nanotech.* **13**, 806 (2018).
- [18] R. S. DiMatteo, P. Greiff, S. L. Finberg, K. A. Young-Waite, H. K. H. Choy, M. M. Masaki, and C. G. Fonstad, Enhanced photogeneration of carriers in a semiconductor via coupling across a nonisothermal nanoscale vacuum gap, *Appl. Phys. Lett.* **79**, 1894 (2001).
- [19] J. Yang, W. Du, Y. Su, Y. Fu, S. Gong, S. He, and Y. Ma, Observing of the super-Planckian near-field thermal radiation between graphene sheets, *Nat. Commun.* **9**, 4033 (2018).
- [20] N. Vongsoasup and K. Hanamura, Effects of near-field radiation and hyperbolic modes on a TPV system, *Therm. Sci. Eng.* **26**, 29 (2018).
- [21] R. B. Godfrey and M. A. Green, 655 mV open-circuit voltage, 17.6% efficient silicon MIS solar cells, *Appl. Phys. Lett.* **34**, 790 (1979).
- [22] R. Hezel, Recent progress in MIS solar cells, *Prog. Photovoltaic Res. Appl.* **5**, 109 (1997).
- [23] L.-C. Liou and B. Nabet, Simple analytical model of bias dependence of the photocurrent of metal–semiconductor–metal photodetectors, *Appl. Opt.* **35**, 15 (1996).
- [24] M. Farhat, S. Kais, and F. Alharbi, Plasmonically enhanced schottky photovoltaic devices, *Sci. Rep.* **7**, 14253 (2017).
- [25] K. W. Johnston, A. G. Pattantyus-Abraham, J. P. Clifford, S. H. Myrskog, S. Hoogland, H. Shukla, E. J. D. Klem, L. Levina, and E. H. Sargent, Efficient Schottky-quantum-dot photovoltaics: Theroles of depletion, drift, and diffusion, *Appl. Phys. Lett.* **92**, 122111 (2008).
- [26] C. Scales and P. Berini, Thin-film Schottky barrier photodetector models, *IEEE J. Quantum Electron.* **46**, 633 (2010).
- [27] R. Sundararaman, P. Narang, A. S. Jermyn, W. A. Goddard III, and H. A. Atwater, Theoretical predictions for hot-carrier generation from surface plasmon decay, *Nat. Commun.* **5**, 5788 (2014).
- [28] M. Bernardi, J. Mustafa, J. B. Neaton, and S. G. Louie, Theory and computation of hot carriers generated by surface plasmon polaritons in noble metals, *Nat. Commun.* **6**, 7044 (2015).
- [29] E. Blandre, D. Jalas, A. Y. Petrov, and M. Eich, Limit of efficiency of generation of hot electrons in metals and their injection inside a semiconductor using a semiclassical approach, *ACS Photonics* **5**, 3613 (2018).
- [30] M. Francoeur, M. P. Mengüç, and R. Vaillon, Solution of near-field thermal radiation in one-dimensional layered media using dyadic Green’s functions and the scattering matrix method, *J. Quant. Spectrosc. Radiat. Transfer* **110**, 2002 (2009).
- [31] E. D. Palik, *Handbook of Optical Constants of Solids* (Academic Press, New York, 1985), Vol. 1.
- [32] A. D. Rakić, A. B. Djurisić, J. M. Elazar, and M. L. Majewski, Optical properties of metallic films for vertical-cavity optoelectronic devices, *Appl. Opt.* **37**, 5271 (1998).
- [33] J. A. González-Cuevas, T. F. Refaat, M. N. Abedin, and H. E. Elsayed-Ali, Modeling of the temperature-dependent spectral response of $In_{1-x}Ga_xSb$ infrared photodetectors, *Opt. Eng.* **45**, 044001 (2006).
- [34] S. Adachi, Optical dispersion relations for GaP, GaAs, GaSb, InP, InAs, InSb, $Al_xGa_{1-x}As$, and $In_{1-x}Ga_xAs_yP_{1-y}$, *J. Appl. Phys.* **66**, 6030 (1989).
- [35] M. Patrini, G. Guizzetti, M. Galli, R. Ferrini, A. Bosacchi, S. Franchi, and R. Magnanini, Optical functions of bulk and epitaxial GaSb from 0.0025 to 6 eV, *Solid State Commun.* **101**, 93 (1997).
- [36] R. F. Pierret, *Semiconductor Device Fundamentals* (Pearson Education, MA, 1996).
- [37] E. H. Rhoderick, Metal-semiconductor contacts, *IEE Proc.* **129**, 1 (1982).
- [38] S. Parui, K. G. Rana, L. Bignardi, P. Rudolf, B. J. van Wees, and T. Banerjee, Comparison of hot-electron transmission in ferromagnetic Ni on epitaxial and polycrystalline Schottky interfaces, *Phys. Rev. B* **85**, 235416 (2012).
- [39] See Supplemental Material at <http://link.aps.org/supplemental/10.1103/PhysRevApplied.11.044040> for discussion of the internal photoemission quantum efficiency, validation of the performance analysis model, and performance dependence on the vacuum gap distance and the emitter temperature.
- [40] S. Basu and Z. M. Zhang, Ultrasmall penetration depth in nanoscale thermal radiation, *Appl. Phys. Lett.* **95**, 133104 (2009).
- [41] B. Song, Y. Ganjeh, S. Sadat, D. Thompson, A. Fiorino, V. Fernández-Hurtado, J. Feist, F. J. García-Vidal, J. C. Cuevas, P. Reddy, and E. Meyhofer, Enhancement of near-field radiative heat transfer using polar dielectric thin films, *Nat. Nanotech.* **10**, 253 (2015).
- [42] Y. Tsurimaki, P.-O. Chapuis, J. Okajima, A. Komiya, S. Maruyama, and R. Vaillon, Coherent regime and far-to-near-field transition for radiative heat transfer, *J. Quant. Spectrosc. Radiat. Transfer* **187**, 310 (2017).
- [43] T. J. Bright, L. P. Wang, and Z. M. Zhang, Performance of near-field thermophotovoltaic cells enhanced with a backside reflector, *J. Heat Transfer* **136**, 062701 (2014).
- [44] O. Vigil-Galán, J. N. Ximello-Quiébras, J. Aguilar-Hernández, G. Contreras-Puente, A. Cruz-Orea, J. G. Mendoza-Álvarez, J. A. Cardona-Bedoya, C. M. Ruiz, and V. Bermúdez, Passivation properties of CdS thin films grown by chemical bath deposition on GaSb: The influence of the S/Cd ratio in the solution and of the CdS layer thickness on the surface recombination velocity, *Semicond. Sci. Technol.* **21**, 76 (2006).

- [45] C. R. Crowell, W. G. Spitzer, L. E. Howarth, and E. E. LaBate, Attenuation length measurements of hot electrons in metal films, *Phys. Rev.* **127**, 2006 (1962).
- [46] G. Fuster, J. M. Tyler, N. E. Brener, J. Callaway, and D. Bagayoko, Electronic structure and related properties of silver, *Phys. Rev. B* **42**, 7322 (1990).
- [47] B. J. Lee, K. Park, T. Walsh, and L. Xu, Radiative heat transfer analysis in plasmonic nanofluids for direct solar thermal absorption, *J. Sol. Energy Eng.* **134**, 021009 (2012).
- [48] T. P. Otanicar, P. E. Phelan, R. S. Prasher, G. Rosenzgarten, and R. A. Taylor, Nanofluid-based direct absorption solar collector, *J. Renew. Sustain. Energy* **2**, 033102 (2010).
- [49] C. L. Nehl, N. K. Grady, G. P. Goodrich, F. Tam, N. J. Halas, and J. H. Hafner, Scattering spectra of single gold nanoshells, *Nano Lett.* **4**, 2355 (2004).
- [50] D. Gall, Electron mean free path in elemental metals, *J. Appl. Phys.* **119**, 085101 (2016).